

Physics-Aware Motion Simulation for T₂*-Weighted Brain MRI

Hannah Eichhorn^{1,2,*}, Kerstin Hammernik², Veronika Spieker^{1,2}, Samira M. Epp^{3,4}, Daniel Rueckert^{2,3,5}, Christine Preibisch³, and Julia A. Schnabel^{1,2,6}

¹ Institute of Machine Learning in Biomedical Imaging, Helmholtz Munich, Germany,

² School of Computation, Information and Technology, Technical University of Munich, Germany

³ School of Medicine, Technical University of Munich, Germany

⁴ Graduate School of Systemic Neurosciences, Ludwig-Maximilians-University, Germany

⁵ Department of Computing, Imperial College London, United Kingdom

⁶ School of Biomedical Engineering and Imaging Sciences, King's College London, United Kingdom

*hannah.eichhorn@helmholtz-munich.de

Abstract. In this work, we propose a realistic, physics-aware motion simulation procedure for T₂*-weighted magnetic resonance imaging (MRI) to improve learning-based motion correction. As T₂*-weighted MRI is highly sensitive to motion-related changes in magnetic field inhomogeneities, it is of utmost importance to include physics information in the simulation. Additionally, current motion simulations often only assume simplified motion patterns. Our simulations, on the other hand, include real recorded subject motion and realistic effects of motion-induced magnetic field inhomogeneity changes. We demonstrate the use of such simulated data by training a convolutional neural network to detect the presence of motion in affected k-space lines. The network accurately detects motion-affected k-space lines for simulated displacements down to ≥ 0.5 mm (accuracy on test set: 92.5%). Finally, our results demonstrate exciting opportunities of simulation-based k-space line detection combined with more powerful reconstruction methods.

Keywords: Brain MRI · Motion Artefacts · Motion Detection · Motion Correction · Deep Learning.

1 Introduction

T₂* quantification, as part of the multi-parametric quantitative BOLD (mqBOLD) protocol [9], enables oxygenation sensitive brain magnetic resonance imaging (MRI) and is more affordable and less invasive than positron emission tomography techniques. Quantitative MRI, as opposed to the more widely used qualitative structural imaging, allows for a consistent extraction of biomarkers across scanners and hospitals by measuring physical tissue properties. Promising applications of the quantitative mqBOLD technique comprise stroke, glioma and

internal carotid artery stenosis [6,12,19]. Motion artefacts, however, remain a major challenge for brain MRI in general. Specifically, T_2^* -weighted gradient echo (GRE) MRI, shows a high sensitivity towards magnetic field (B_0) inhomogeneities and is hence particularly affected by subject head motion [16]. Due to the increasing impact of motion with increasing echo times, motion severely affects the signal decay over several echoes and, thus, the accuracy of the T_2^* quantification from multi-echo data [17]. Artefacts have been shown to propagate from the T_2^* mapping towards derived parameters even for mild motion with less than 1 mm average displacements during the scans [5], which underlines the need of intra-scan motion correction (MoCo) for T_2^* -weighted GRE data.

Deep learning solutions have shown promising results for correcting motion in various MR applications. MoCo has been approached as an image denoising problem, using convolutional neural networks [3,24] as well as generative adversarial networks [11,14]. However, acting purely on image data, such methods cannot guarantee consistency with the acquired raw k-space data, which might hinder their translation into clinical practice. Enforcing data consistency is only possible when combining MoCo with the image reconstruction process [8,18,20]. Yet, the majority of learning-based MoCo techniques - whether purely image-based or combined with the reconstruction process - rely on the availability of paired motion-free and motion-corrupted data for supervised model training [22]. Since the acquisition of large paired datasets is expensive and not always feasible, motion simulation is widely used. However, realistic and physics-aware simulations are still underutilised. Some authors merely exchange k-space lines between different time points [18]. Others use MR physics as basis for a more realistic simulation, but only combine a small number of discrete motion states, ignoring the continuous nature of real subject motion [3,11,20,24]; or only simulate in-plane motion instead of realistic 3D motion [3,20]. Furthermore, second-order motion effects like motion-induced magnetic field changes are commonly ignored.

In this work, we propose a physics-aware motion simulation procedure that allows for more realistic model training in the presence of magnetic field inhomogeneities and demonstrate its use for the learning-based detection of motion-corrupted k-space lines in T_2^* -weighted MRI. Our contributions are three-fold:

1. We carry out realistic motion simulations based on real recorded patient motion. In contrast to state-of-the-art methods, we do not only include rigid-body transformations, but also B_0 inhomogeneities as second-order effects.
2. Inspired by the work of Oksuz et al. [18], we train a 3D convolutional neural network to classify individual motion-affected k-space lines, leveraging the multi-echo information of the T_2^* -weighted brain dataset.
3. To demonstrate the potential of our work, we show motion corrected images where information on motion-affected lines is included as a weighting mask in the data consistency term of the iterative reconstruction procedure.

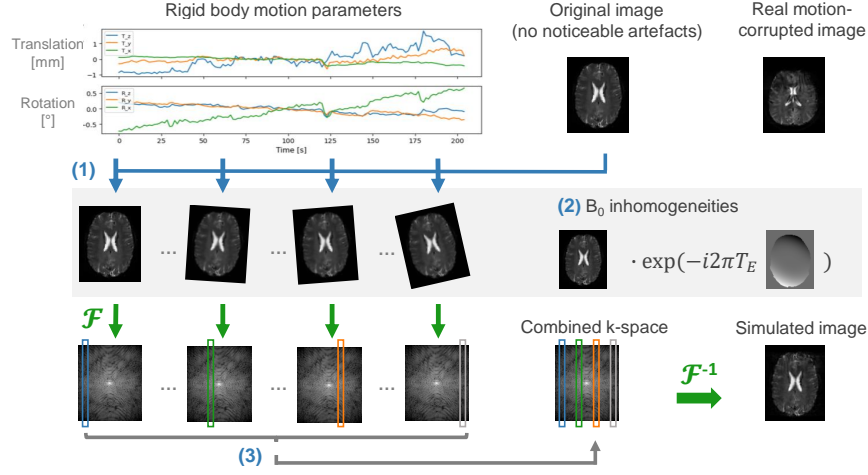


Fig. 1. Visualisation of the motion simulation approach. (1) Rigid-body transformations are applied to the complex original image data for each time point. (2) A phase term with randomly generated B_0 inhomogeneities is multiplied to the transformed images. The results are transformed into k-space. (3) k-Space lines from the individual motion states are merged into the final simulated k-space, accounting for the multi-slice acquisition scheme. An inverse Fourier transform yields the motion corrupted image.

2 Methods

2.1 Motion Simulation

The MRI single coil forward model in the presence of rigid-body motion includes the Fourier transform \mathcal{F} , the sampling mask \mathbf{M}_t and the three parameter rotation and translation transforms, \mathbf{R}_t and \mathbf{T}_t , which are applied to the motion-free image x for each time point t , yielding the motion-affected k-space data y [1]:

$$y = \sum_{t=1}^T \mathbf{M}_t \mathcal{F} \mathbf{T}_t \mathbf{R}_t x. \quad (1)$$

As second-order motion effect, we further include a phase shift, which is induced by position-dependent magnetic field inhomogeneities $\omega_{\mathbf{B}_0 t}$ and increases with the echo time T_E :

$$y = \sum_{t=1}^T \mathbf{M}_t \mathcal{F} e^{-2i\pi\omega_{\mathbf{B}_0 t} T_E} \mathbf{T}_t \mathbf{R}_t x. \quad (2)$$

Based on this, motion is simulated by rigidly transforming the complex MRI data and subsequently merging different motion states in k-space, as visualised in Fig. 1. In this process, the actual multi-slice acquisition scheme is considered, i.e. the ordering of phase encoding lines is included in \mathbf{M}_t . Additionally, for time

points with average displacements of more than 0.5 mm, magnetic field inhomogeneities are incorporated by multiplying the image with a B_0 map that was modified by adding random image gradients with deviations of max. 5 Hz [15].

Motion simulation is only performed for phase encoding (PE) lines, where the average displacement of points within a sphere with radius 64 mm, as model of the head, exceeds a certain threshold value d_{min} . To investigate the amount of motion that can be detected, this so-called *simulation threshold* is varied between 0.25 mm and 1.0 mm in the experiments. To avoid the need of registration for calculating full-reference metrics with respect to the original motion-free image, the motion curves are transformed in a way that the median motion state - measured by the average displacement - is in the zero-position.

2.2 k-Space Line Classification Network

The line classification network is adapted from Oksuz et al. [18] and consists of five repetitions of 3D convolution, batch normalisation, ReLU activation, dropout and max pooling layers, followed by a fully connected, a dropout and a sigmoid activation layer, as visualised in Fig. S1 of the Supplementary Material. Convolution layers are implemented with a kernel size of $3 \times 3 \times 3$. Max pooling is performed in the echo and readout dimensions. The network is trained for 300 epochs with Adam [13] using a learning rate of 5×10^{-4} and a weighted cross entropy loss between prediction m^{pr} and target m^{ta} :

$$L(m^{pr}, m^{ta}) = -m^{ta} \log(m^{pr} + \epsilon) - \omega \cdot (1 - m^{ta}) \log((1 - m^{pr}) + \epsilon). \quad (3)$$

Weights of the epoch with the lowest validation loss are used. Batch sizes of 32 and 64, weighting factors, ω , between 1 and 5, weight decays between 1×10^{-5} and 5×10^{-2} and dropout probabilities between 10% and 30% are tested and the best configuration is chosen based on the validation dataset (64 / 5 / 1×10^{-3} / 20%; 219,380 trainable parameters). The average runtime of the network training is 14 hours. Computations are performed on an NVIDIA RTX A6000, using Python 3.8.12 and PyTorch 1.13.0 (code available at: <https://github.com/HannahEichhorn/T2starLineDet>).

2.3 Data

Motion simulation for training and evaluation of the line classification network is performed on 116 complex, coil-combined T_2^* -weighted datasets of 59 healthy volunteers, which can be expected to not considerably move during the scanning. We visually confirmed that these data did not show noticeable motion artefacts. The unpublished mqBOLD data originates from four ongoing studies investigating brain oxygen metabolism on a 3T Philips Elition MR scanner (Philips Healthcare, Best, The Netherlands), using a multi-slice GRE sequence (12 echoes, 30-36 slices, $TE1/\Delta TE = 5/5$ ms, $TR=1910-2291$ ms, $\alpha=30^\circ$, voxel size: $2 \times 2 \times 3$ mm³). The ongoing studies have been approved by the local ethics committee (approval numbers 472/16 S, 446/21 S, 165/21 S, 382/18 S). The

available datasets are divided subject-wise into train, validation and test sets (74/18/24 datasets).

For a realistic motion simulation, we base our simulation on real head motion. We extract 132 motion curves of length 235 s from 62 functional MRI (fMRI) time series (unpublished data from two ongoing studies, independent cohorts from above imaging cohorts). These are divided into train, validation and test sets ($N = 88/20/24$ motion curves), keeping the amount of motion as equal as possible in the different sets. Principal component analysis is used to determine the largest modes of variations of the training motion curves $pc_i(t)$, which are combined with random weights α_i and added to the mean curve $T(t)$ to generate augmented training samples [4]:

$$T_{new}(t) = \overline{T(t)} + \sum_{i=1}^{0.2 \cdot N} \alpha_i \cdot pc_i(t). \quad (4)$$

For each complex image in the training set, six motion curves are generated for simulation. Slices with more than 30% background voxels are excluded. This results in a total of 8,922 slices for training, 392 for validation and 492 for testing.

Preprocessing: The complex data are normalised for each line individually:

$$y_{ep}^n = \frac{y_{ep}}{\sqrt{\sum_{ep} |y_{ep}|^2}}, \quad (5)$$

with e , p and r indicating the echo, phase encoding and readout dimension. Real and imaginary parts are fed into the network as different channels.

The target classification labels are calculated by thresholding and inverting the average displacement of a sphere with a 64 mm radius at the acquisition time of the corresponding PE line, using the simulation threshold value d_{min} . The target masks are averaged across all 12 echoes, since these have been acquired within 60 ms and are thus assumed to have been acquired during the same motion state.

2.4 Evaluation

The predicted classification labels are evaluated based on accuracy, corresponding to the rate of correctly predicted lines. For a more detailed interpretation, the rate of non-detected lines (ND) is calculated as the fraction of lines with motion ($m^{ta} = 0$), which the network does not detect ($m^{pr} = 1$). Similarly, the rate of wrongly-detected lines (WD) is calculated as the fraction of lines without motion ($m^{ta} = 1$), which the network classifies as motion-corrupted ($m^{pr} = 0$).

2.5 Weighted Iterative Reconstruction

Inspired by the work of Jiang et al. [10], we include the estimated motion classification as weights into the data consistency (DC) term of the single coil MRI

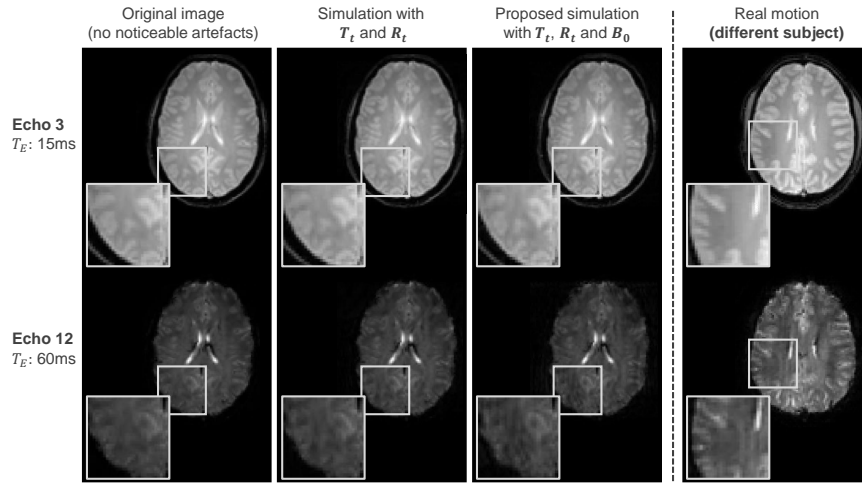


Fig. 2. Example images showing the relevance of B_0 inhomogeneities for generating realistic artefact patterns. From left to right: original images (without noticeable motion artefacts), simulated images without and with B_0 inhomogeneities and real motion images for two different echo times (top and bottom row). The motion curve for the simulation is shown in Fig. S2 of the Supplementary Material (mean displacement during the whole scan: 0.89 mm, simulation threshold: 0.5 mm). Artefacts - i.e. blurring of underlying structures and wave-like patterns - are more pronounced for later echoes in the real motion case and in the proposed simulation method.

reconstruction model with total variation (TV) regularisation:

$$x^* = \arg \min_x \frac{1}{2} \| \mathbf{W}(\mathbf{A}x - y) \|_2^2 + \lambda \| \Phi x \|_1 . \quad (6)$$

\mathbf{W} represents a diagonal matrix with empirical weights, 0.25 or 1 for the presence or absence of motion in each PE line, $\mathbf{A} = \mathcal{F}$ the forward operator, $\lambda = 2$ the regularisation parameter obtained empirically and Φ the finite differences operator. Eq. 6 can be solved for the optimal x^* with a proximal gradient algorithm [7].

3 Experiments and Results

In Fig. 2 we visually compare simulations of motion-affected images without and with B_0 inhomogeneities with a real motion case. This example demonstrates the relevance of including motion-induced field inhomogeneity changes for generating realistic artefact patterns, i.e. more severe blurring and wave-like artefacts appearing for later echoes.

In the following, we use the simulated data to investigate the minimal level of simulated motion, which can be detected by the line classification network. We train the network using four different datasets which were simulated with varying simulation thresholds d_{min} . Fig. 3 compares accuracy, ND and WD rates

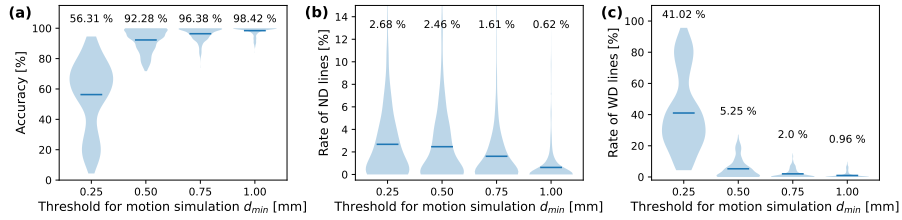


Fig. 3. (a) Test accuracy, (b) rates of non-detected (ND) and (c) wrongly-detected (WD) k-space lines for varying thresholds of simulated motion in train and test data. Mean values are visualised by horizontal lines and given in numbers. All metrics show a decreasing classification performance with decreasing simulation thresholds.

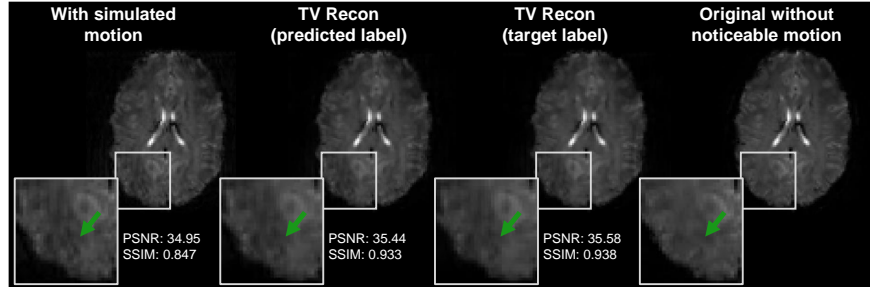


Fig. 4. Demonstration of weighted reconstructions for simulated data. From left to right: images with simulated motion (same data as in Fig. 2, simulation threshold: 0.5 mm), TV reconstructions weighted with predicted labels by the network as well as target labels, and original images. Peak signal-to-noise ratio (PSNR) and structural similarity index (SSIM) [23] with respect to the original images are given below the images. Green arrows indicate an area with subtly reduced artefacts in the weighted reconstructions.

of these networks’ predictions on unseen test data (with the same simulation thresholds as for training). The performance in terms of accuracy, ND and WD rate decreases for training and testing the networks with decreasing simulation thresholds. When changing the simulation threshold from 0.5 mm to 0.25 mm, the accuracy drops from 92.28% to 56.31%, which is mainly driven by an increase of the WD rate from 5.25% to 41.02%. This indicates that the network is not able to correctly classify motion-affected PE lines when motion is simulated for time points with less than 0.5 mm average displacement of a 64 mm sphere.

As an outlook, Fig. 4 demonstrates that the predicted line-wise classification labels can be used for correcting motion-corrupted images by including the classifications as weights in the DC term of the reconstruction model (Eq. 6). Visual inspection reveals a subtle decrease of motion artefacts in the weighted reconstruction with target labels and to a certain extent also in the reconstruction with predicted labels. This is in agreement with an improvement of quantita-

tive metrics for both scenarios. However, the weighted reconstructions appear slightly over-smooth compared to the original image.

4 Discussion

We have proposed a physics-aware method to realistically simulate motion artefacts for T_2^* -weighted brain MRI in the presence of magnetic field inhomogeneities, which enables supervised training of MoCo models, and, thus, avoids the expensive acquisition of paired in-vivo data. We demonstrated the use of such simulated data for training a k-space line detection network and showed a usecase of this approach for a motion-corrected reconstruction.

Most learning-based MoCo approaches rely on simplistic motion simulation for supervised model training. Oksuz et al. [18], for instance, simulate motion in dynamic cardiac MRI as mistriggering artefacts by exchanging k-space lines between different time points, which does not cover the full range of possible motion artefacts. Others use the MR forward model (Eq. 1) as basis for a more realistic simulation, but only merge a few, discrete motion states and, thus, ignore the continuous nature of real subject motion [3,11,20,24]; or only simulate in-plane motion instead of realistic 3D motion [3,20]. To improve the performance of the developed algorithms on real motion data, the training data generation needs to be as realistic as possible. Thus, our proposed simulation is based on real recorded 3D subject head motion extracted from fMRI time series. Furthermore, due to the sensitivity of T_2^* -weighted GRE to magnetic field inhomogeneities, our physics-aware simulation incorporates B_0 inhomogeneity changes as secondary motion effects in addition to rigid-body transformations.

The comparison of simulation examples with a real motion case in Fig. 2 demonstrated that the proposed inclusion of B_0 changes in the simulation results in more plausible artefact patterns. Note that - due to inherently long acquisition times - the resolution of quantitative MRI (with typical voxel sizes of 2-3 mm) is commonly lower than for qualitative structural MRI (e.g. T1-weighted MPRAGE scans with voxel sizes < 1 mm). Furthermore, the shown motion artefacts, which mainly manifest in blurring and wave-like patterns, might not appear as severe as in previous studies, where authors simulated motion considerably larger than a voxel size [8,11,14]. However, MoCo is required even for more cooperative subjects in the context of T_2^* quantification based on multi-echo GRE data. That is because motion and associated B_0 changes disturb the signal decay over several echo times, even for displacements smaller than the voxel size of 2 mm [5].

To showcase the use of the proposed simulation, we trained a convolutional neural network to detect the presence or absence of motion for every k-space line. First, we have investigated the extent of motion that can be detected by the network. For this, we have varied the simulation threshold for both training and test data. The network was able to classify displacements down to 0.5 mm, corresponding to one quarter of the voxel size, with an accuracy of 92.3%. For smaller simulation thresholds, we have observed a clear performance drop. Considering that the underlying motion curves were extracted from real fMRI time

series, a certain degree of noise due to the co-registration can be expected for very small displacements. Thus, using such motion information in the simulation might lead to an overestimation of motion artefacts, which justifies to simulate motion only for time points with displacements larger than 0.5 mm.

As proof-of-principle, we have included the classification labels as weights in the DC term of an iterative reconstruction and demonstrated how the detected motion information can be used for MoCo. The results showed subtly reduced motion artefacts, both visually and quantitatively. However, the reconstructions appeared slightly over-smoothed compared to the original image, which is a common problem when using TV regularisation. In future work we plan to combine line-wise classifications as DC weights with e.g. learning an unrolled optimisation scheme [21]. We further plan to utilise multi-coil raw k-space data to exploit redundancies between coils for improved reconstruction performance.

One limitation of the proposed motion simulation procedure is that we generated random B_0 inhomogeneity variations for each position. More authentic, pose-dependent B_0 inhomogeneity maps can be synthesized by interpolating between B_0 fields of the same subject acquired in different positions [2]. This requires repeated measurements of each subject in different positions, though, which is not feasible for generating large-scale training datasets. Finally, an evaluation of the trained network using real motion corrupted data remains for future work. We just received ethics approval to perform paired in-vivo experiments, which will allow for more thorough quantitative evaluations.

Conclusion We have presented a method for realistic, physics-based motion simulation in T2*-weighted GRE MRI. Our proposed method uses motion curves extracted from real, time-resolved fMRI data and includes motion induced changes in B_0 inhomogeneities. We demonstrated the utility of these simulations for training a line-wise classification network and have been able to detect displacements down to 0.5 mm (a quarter of a voxel). Finally, we outlined how the simulation-based motion detection might be included in the data consistency term of an iterative reconstruction procedure, providing a promising research direction for future work.

Acknowledgements

V.S. and H.E. are partially supported by the Helmholtz Association under the joint research school "Munich School for Data Science - MUDS".

References

1. Retrospective correction of motion in MR images. In: van der Kouwe, A.J., Andre, J.B. (eds.) *Motion Correction in MR*, vol. 6, pp. 259–267. Academic Press (2022)
2. Brackenier, Y., Cordero-Grande, L., Tomi-Tricot, R., Wilkinson, T., Bridgen, P., Price, A., Malik, S.J., De Vita, E., Hajnal, J.V.: Data-driven motion-corrected brain MRI incorporating pose-dependent B_0 fields. *Magnetic Resonance in Medicine* **88**(2), 817–831 (2022)

3. Chatterjee, S., Sciarra, A., Dünnwald, M., Oeltze-Jafra, S., Nürnberger, A., Speck, O.: Retrospective motion correction of MR images using prior-assisted deep learning. In: Proceedings of the 34th Conference on NeurIPS (2020)
4. Cootes, T.F., Taylor, C.J., Cooper, D.H., Graham, J.: Active shape models - their training and application. *Computer Vision and Image Understanding* **61**(1), 38–59 (1995)
5. Eichhorn, H., Hammernik, K., Epp, S.M., Karampinos, D.C., Schnabel, J.A., Preibisch, C.: Investigating the impact of motion and associated B0 changes on oxygenation sensitive MRI through realistic simulations. In: Proc. Intl. Soc. Mag. Reson. Med. vol. 31 (2023)
6. Gersing, A.S., Ankenbrank, M., Schwaiger, B.J., Toth, V., Janssen, I., Kooijman, H., Wunderlich, S., Bauer, J.S., Zimmer, C., Preibisch, C.: Mapping of cerebral metabolic rate of oxygen using dynamic susceptibility contrast and blood oxygen level dependent MR imaging in acute ischemic stroke. *Neuroradiology* **57**, 1253–1261 (2015)
7. Hammernik, K., Knoll, F.: Machine learning for image reconstruction. In: Zhou, S.K., Rueckert, D., Fichtinger, G. (eds.) *Handbook of Medical Image Computing and Computer Assisted Intervention*, pp. 25–64. Academic Press (2020)
8. Haskell, M.W., Cauley, S.F., Bilgic, B., Hossbach, J., Splitthoff, D.N., Pfeuffer, J., Setsompop, K., Wald, L.L.: Network accelerated motion estimation and reduction (NAMER): Convolutional neural network guided retrospective motion correction using a separable motion model. *Magnetic Resonance in Medicine* **82**(4), 1452–1461 (2019)
9. Hirsch, N.M., Toth, V., Förschler, A., Kooijman, H., Zimmer, C., Preibisch, C.: Technical considerations on the validity of blood oxygenation level-dependent-based MR assessment of vascular deoxygenation: Bold-based assessment of vascular deoxygenation. *NMR in Biomedicine* **27**(7), 853–862 (2014)
10. Jiang, W., Ong, F., Johnson, K.M., Nagle, S.K., Hope, T.A., Lustig, M., Larson, P.E.Z.: Motion robust high resolution 3D free-breathing pulmonary MRI using dynamic 3D image self-navigator. *Magnetic Resonance in Medicine* **79**(6), 2954–2967 (2018)
11. Johnson, P.M., Drangova, M.: Conditional generative adversarial network for 3D rigid-body motion correction in MRI. *Magnetic Resonance in Medicine* **82**(3), 901–910 (2019)
12. Kaczmarz, S., Göttler, J., Petr, J., Hansen, M.B., Mouridsen, K., Zimmer, C., Hyder, F., Preibisch, C.: Hemodynamic impairments within individual watershed areas in asymptomatic carotid artery stenosis by multimodal MRI. *Journal of Cerebral Blood Flow & Metabolism* **41**(2), 380–396 (2021)
13. Kingma, D.P., Ba, J.: Adam: A method for stochastic optimization. In: Proceedings of the 3rd ICLR (2015)
14. Küstner, T., Armanious, K., Yang, J., Yang, B., Schick, F., Gatidis, S.: Retrospective correction of motion-affected MR images using deep learning frameworks. *Magnetic Resonance in Medicine* **82**(4), 1527–1540 (2019)
15. Liu, J., de Zwart, J.A., van Gelderen, P., Murphy-Boesch, J., Duyn, J.H.: Effect of head motion on MRI B0 field distribution. *Magnetic Resonance in Medicine* **80**(6), 2538–2548 (2018)
16. Magerkurth, J., Volz, S., Wagner, M., Jurcoane, A., Anti, S., Seiler, A., Hattin-gen, E., Deichmann, R.: Quantitative T2* -mapping based on multi-slice multiple gradient echo flash imaging: Retrospective correction for subject motion effects: Movement correction in T2* mapping. *Magnetic Resonance in Medicine* **66**(4), 989–997 (2011)

17. Nöth, U., Volz, S., Hattingen, E., Deichmann, R.: An improved method for retrospective motion correction in quantitative T2* mapping. *NeuroImage* **92**, 106–119 (2014)
18. Oksuz, I., Clough, J.R., Ruijsink, B., Anton, E.P., Bustin, A., Cruz, G., Prieto, C., King, A.P., Schnabel, J.A.: Deep learning-based detection and correction of cardiac MR motion artefacts during reconstruction for high-quality segmentation. *IEEE Transactions on Medical Imaging* **39**(12), 4001–4010 (2020)
19. Preibisch, C., Shi, K., Kluge, A., Lukas, M., Wiestler, B., Göttler, J., Gempt, J., Ringel, F., Al Jaber, M., Schlegel, J., et al.: Characterizing hypoxia in human glioma: a simultaneous multimodal MRI and PET study. *NMR in Biomedicine* **30**(11), e3775 (2017)
20. Rotman, M., Brada, R., Beniaminy, I., Ahn, S., Hardy, C.J., Wolf, L.: Correcting motion artifacts in MRI scans using a deep neural network with automatic motion timing detection. In: *Medical Imaging 2021: Physics of Medical Imaging*. vol. 11595, pp. 296–305. SPIE (2021)
21. Schlemper, J., Caballero, J., Hajnal, J.V., Price, A.N., Rueckert, D.: A deep cascade of convolutional neural networks for dynamic MR image reconstruction. *IEEE Transactions on Medical Imaging* **37**(2), 491–503 (2018)
22. Spieker, V., Eichhorn, H., Hammernik, K., Rueckert, D., Preibisch, C., Karampinos, D.C., Schnabel, J.A.: Deep learning for retrospective motion correction in MRI: A comprehensive review, arXiv: 2305.06739
23. Wang, Z., Bovik, A., Sheikh, H., Simoncelli, E.: Image quality assessment: from error visibility to structural similarity. *IEEE Transactions on Image Processing* **13**(4), 600–612 (2004)
24. Xu, X., Kothapalli, Satya V. V. N., Liu, J., Kahali, S., Gan, W., Yablonskiy, D.A., Kamilov, U.S.: Learning-based motion artifact removal networks for quantitative R2* mapping. *Magnetic Resonance in Medicine* **88**(1), 106–119 (2022)

Supplementary Material

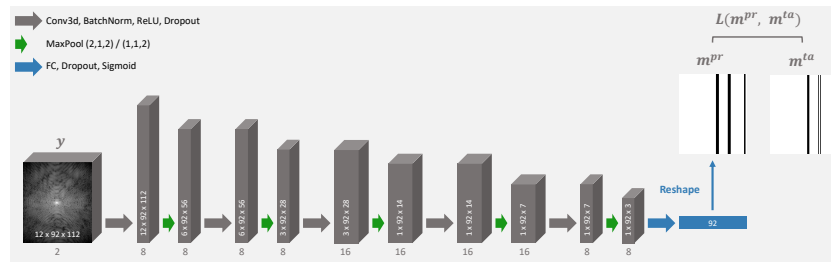


Fig. S1. Network architecture for line-wise classification. Input y of the network is the motion corrupted k-space. The 219,380 trainable parameters are updated based on the loss calculated between the predicted and the target classification, m^{pr} and m^{ta} , which are visualised in black or white for the presence or absence of motion in each PE line.

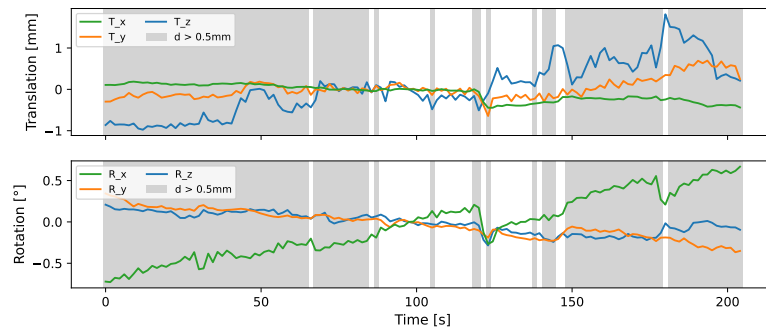


Fig. S2. Motion parameter curves used in the simulation of the example images shown in Figs. 2 and 4 of the main article (mean displacements during the whole scan: 0.89 mm). Translations along x-, y- and z-axis are shown in the top row, rotations around x-, y- and z-axis in the bottom row. Grey background represents time points with displacements, d , larger than 0.5 mm, which corresponds to time points, for which motion was simulated.